V European Conference on Computational Fluid Dynamics
ECCOMAS CFD 2010
J. C. F. Pereira and A. Sequeira (Eds)
Lisbon, Portugal, 14-17 June 2010

ADJOINT RANS FOR AFTSHIP DESIGN

Arthur Stück*, Jörn Kröger and Thomas Rung

Institute for Fluid Dynamics and Ship Theory
Hamburg University of Technology
Schwarzenbergstraße 95, D-21073 Hamburg
*e-mail: arthur.stueck@tu-harburg.de

Key words: Adjoint RANS, Hull Shape Design, Ship Wake, Unstructured Grids, Finite Volume Method

Abstract. *Aided by the RANS-based continuous adjoint sensitivity analysis, two hull forms – a simple submersed body and a container vessel – are re-designed in order to improve their propeller wake field. The re-design is carried out manually at model-scale guided by the sensitivity information. Two wake objective functions are introduced to the adjoint method for the calculation of hydrodynamic shape sensitivities. Both flow and adjoint solvers are based on an unstructured finite-volume discretisation for incompressible flow. When visualised properly, the continuous sensitivity distribution yields considerable insight into the design problem from the objective point of view.*

1 INTRODUCTION

Shape design is one of the most important drivers for the use of CFD in marine industry. Continuous improvements of computer performance and algorithm efficiency allow for viscous computations in the framework of practical ship design. CFD brings a competitive advantage when it guides the analyst to a better design. Engineers need to understand the dependence of the design objectives $J_i\,(1 < i < n_J)$ on the flow which, in turn, depends on the shape $b_k\,(1 < k < n_b)$. Sensitivity derivatives of the objective function with respect to the shape describe the dependence in a linear sense. When many design parameters are involved in the optimisation, the computational effort for the sensitivity analysis quickly becomes prohibitive. Direct techniques, such as finite differencing, the direct linearisation approach or the complex variable method require of the order $O(n_b)$ objective function evaluations. Other the adjoint method, that yields the sensitivity derivatives roughly at the expense of one CFD run, i.e. independent of the number of parameters. The method was pioneered by Lions[1] and Pironneau[2] and established by Jameson[3] in aerodynamic design. In the publications[4–8] the focus is on hydrodynamic applications and incompressible flow.

We have preferred the continuous adjoint (derive-then-discretise) to the discrete adjoint (discretise-then-derive) approach for two reasons: The continuous adjoint equations are derived from the governing RANS equations analytically. Huge portions of the flow solver can be reused in the adjoint solver which significantly reduces the implementation effort. Secondly, the flow solver uses a segregated pressure-correction scheme, that is solved iteratively. Hand-coding of the discrete adjoint is a tedious task for such iterative algorithms, that do not contain coupled Jacobian sub-matrices which could be transposed easily. Automatic differentiation in reverse mode is hardly an alternative in combination with modern software structures. To minimise the turnaround-times (from case set-up to result) in practical shape design, we have used an unstructured grid approach. This significantly reduces the necessary user input during mesh generation when complex topologies are involved.

The remainder of the paper is organised as follows: The wake design problem is introduced in Section 2 outlining the considered wake objective functions. The design is evaluated by the RANS method (Section 3) that is derived to obtain the corresponding adjoint RANS problem (Section 4). Attention then turns to the flow and adjoint solvers (Section 5), followed by applications to a generic submerged body and the KCS container vessel in Sections 6 and 7. A conclusion completes the exposition.

2 WAKE DESIGN

The propeller operates in the so-called *in-behind* condition in the wake field of the ship which differs from the *open-water* condition in an undisturbed, homogeneous, axial inflow. In order to improve the propeller inflow conditions, the *nominal wake field*, denoting the incoming flow aft of the ship without presence of the propeller, is investigated. The flow is evaluated in the propeller disk representing the volume swept by the turning propeller. We use a system of physical cylinder coordinates (r, θ, a) that is located in the centre of the propeller hub

$$x_i\,\underline{e}_i = r\,\tilde{\underline{e}}^r + \theta\,\tilde{\underline{e}}^\theta + a\,\tilde{\underline{e}}^a\,. \tag{1}$$

$\underline{\tilde{e}}^a$ is aligned with the propeller axis pointing from fore to aft. The upright position is described by $\theta = 0$. The corresponding velocity coordinates are U_r, U_θ and U_a. The propeller disk extends over the volume $R_I < r < R_O$, $0 < \theta < 2\pi$, $a_{\text{fore}} < a < a_{\text{aft}}$, where the inner radius R_I is the propeller hub radius and the outer radius R_O is slightly beyond the propeller tip radius. In axial direction the disk reaches from a_{fore} to a_{aft}.

For a single-screw ship, the $\theta = 0$ position is strongly influenced by the presence of the ship hull, while the lower region is usually less affected. In addition, frames with a characteristic U-shape may provoke a bilge vertex that disturbs the flow field in the propeller disk. Two aspects describing the wake quality can be distinguished, being the radial and circumferential variation of the flow. Local deviations in the axial velocity U_a and the tangential velocity component U_θ lead to a local variation of the propeller blade load, due to changes in the blade angle of attack and the magnitude of the inflow velocity. The propeller blades pass wake inhomogeneities at the *blade frequency* which is the number of blades times the number of revolutions. The pressure fields of the passing blades excite the ship structure at the blade frequency and its multiples causing vibrations and noise. This effect is accompanied by cavitation, particularly in the area of highest blade loads and low hydrostatic pressure above the propeller. Bubble growth and collapse lead to pressure pulses at high frequencies. Beyond noise and vibration, cavitation damages may occur on the propeller and the rudder. These devices are particularly sensitive in the context of ship safety and security.

The ship's nominal wake field has to be taken into account during the design of the propeller blade sections. The radial variation of the wake field can be compensated by choosing an appropriate pitch distribution over the radius. The circumferential variation cannot be met by the propeller design. Typically a mean inflow condition is considered for each propeller radius. An appropriate hull shape facilitates the propeller design and improves the propeller-hull interaction.

We have turned the wake design problem into an optimisation problem: Find the hull form parameters b_i that lead to an increased homogeneity of the wake field. The design is evaluated in terms of integral hydrodynamic wake objective functionals J, quantifying the quality of the wake field. The objective functional is obtained by integration over the propeller disk volume or *objective volume* $\Omega_{\text{obj}} \cap \Omega$:

$$J = \int_{\Omega_{\text{obj}}} j \, \mathrm{d}\Omega \,. \tag{2}$$

Among several wake objective functions used in maritime industry is the formulation proposed by the SVA Potsdam.[9] The *SVA criterion* is based on the deviation of the axial velocity component U_a from its mean value $\overline{U}_a(r)$ that is obtained by averaging over the circumference via

$$\overline{U}_a(r) = \frac{1}{2\pi} \int_0^{2\pi} \mathrm{d}\theta \; U_a(r) \qquad \text{for} \quad R_I < r < R_O \,. \tag{3}$$

With U_S denoting the ship velocity, the integral variation for each radius

$$\mathcal{D}_I(r) = \frac{1}{2\,\pi\,U_S} \int_0^{2\pi} \mathrm{d}\theta \; \left| U_a - \overline{U}_a \right| \,, \quad R_I < r < R_O \,, \tag{4}$$

is weighted by the relative bandwidth experienced on that radius

$$\mathcal{D}_{II}(r) = \frac{1}{U_S}\left[\max(U_a) - \min(U_a)\right] , \quad R_I < r < R_O \, . \tag{5}$$

With the definitions above the optimisation goal is to find a hull shape that maximises the wake objective function

$$J_A = 1 - \frac{1}{R_O - R_I}\int_{R_I}^{R_O} \mathrm{d}r \, \sqrt{2\,\mathcal{D}_I(r)\,\mathcal{D}_{II}(r)} \, . \tag{6}$$

In combination with unstructured grids in which the nodes are not aligned with the propeller coordinate system, the wake objective function requires to be re-stated, e.g.

$$J_A = 1 - C_A \int_{\Omega_{\mathrm{obj}}} \frac{\mathrm{d}\Omega}{r} \sqrt{U_S\,\mathcal{D}_{II}(r)\,\left|U_a - \overline{U}_a(r)\right|} \, , \tag{7}$$

with $\mathcal{D}_{II}(r)$ according to Eqn. (5) and

$$C_A = \left[U_S \int_{\Omega_{\mathrm{obj}}} \frac{\mathrm{d}\Omega}{r} \right]^{-1} . \tag{8}$$

The integration is carried out over the computational cells whose centres fall inside the propeller disk volume Ω_{obj}.

A *simplified wake objective function* J_B measures the quadratic deviation in U_a from its radial average, viz. maximise

$$J_B = 1 - C_B \int_{\Omega_{\mathrm{obj}}} \frac{\mathrm{d}\Omega}{2r} \left[U_a - \overline{U}_a(r)\right]^2 \qquad \text{with} \qquad C_B = \left[U_S^2 \int_{\Omega_{\mathrm{obj}}} \frac{\mathrm{d}\Omega}{r} \right]^{-1} . \tag{9}$$

3 RANS-BASED DESIGN EVALUATION

The objective function is determined from the mean velocity components in the propeller disk. The flow, in turn, is subject to the incompressible steady-state RANS equations, which are a reasonable efficiency-accuracy trade-off for aftship design:

$$R_i = \rho \frac{\mathrm{D}U_i}{\mathrm{D}t} - \frac{\partial \pi_{ij}}{\partial x_j} - f_i = 0 \qquad \text{and} \qquad Q = -\frac{\partial U_i}{\partial x_i} = 0 \qquad \text{in} \quad \Omega \, , \tag{10}$$

where U_i, p and f_i denote the mean velocity components, the modified mean pressure and body force components. The hydrodynamic stress tensor is defined as

$$\pi_{ij} = -p\,\delta_{ij} + 2\,\mu_{\mathrm{eff}} S_{ij} \qquad \text{with} \qquad S_{ij} = \frac{1}{2}\left(\frac{\partial U_i}{\partial x_j} + \frac{\partial U_j}{\partial x_i} \right) . \tag{11}$$

The molecular viscosity μ is augmented by the eddy viscosity μ_{T} to give the effective viscosity, $\mu_{\mathrm{eff}} = \mu + \mu_{\mathrm{T}}$. The k-ω-type turbulence models applied determine the eddy viscosity from the turbulent kinetic energy divided by the specific dissipation rate, viz. $\mu_{\mathrm{T}} = \rho\, k/\omega$.

As indicated above the shape of the design surface influences the objective merely via the flow

$$J(\underline{U}(\underline{b}))\,, \tag{12}$$

i.e. the objective function does not depend on the design explicitly. When the design surface $\Gamma_{\mathrm{dsg}} \subset \Gamma$ is subject to a small shape variation δb_i $(i = 1, n_b)$, the interior domain Ω has to follow the perturbation to avoid gaps in the perturbed domain. The rest of the boundaries, $\Gamma \setminus \Gamma_{\mathrm{dsg}}$, remains unchanged. The spatial displacements corresponding to a change in the shape variables b_i are

$$\delta x_k = \sum_{i=1}^{n_b} \left(\delta b_i \frac{\partial x_k}{\partial b_i} \right) \qquad \text{on/in} \quad \Gamma_{\mathrm{dsg}}\,,\ \Omega\,. \tag{13}$$

The shift vector δx_k corresponds to a particular combination of shape parameter variations. Imposing the spatial perturbations (13) on the *old* (subindex 0) domain yields the *new* (subindex 1) position

$$\underline{x}_1 = \underline{x}_0 + \delta\underline{x} \qquad \text{on/in} \quad \Gamma_{\mathrm{dsg}}\,,\ \Omega\,. \tag{14}$$

A modification of the domain induces a change of the flow. With $\phi^{(0)}$ $[\phi^{(1)}]$ referring to the old [new] flow, the new flow at the new position can be written as

$$\phi^{(1)}\big|_{\underline{x}_1} = \phi^{(0)}\big|_{\underline{x}_0} + \sum_{i=1}^{n_b} \delta b_i \left[\underbrace{\frac{\partial \phi}{\partial b_i}}_{\text{loc.}} + \underbrace{\frac{\partial x_k}{\partial b_i} \frac{\partial \phi^{(0)}}{\partial x_k}}_{\text{conv.}} \right]_{\underline{x}_0}\,, \tag{15}$$

containing both *local* and *convective* flow variations. This decomposition accounts for the local flow change $(\delta U_i, \delta p)$ at the old grid position and the spatial, or convective, variation of the old flow due to a nodal position shift δx_i, respectively. The latter is obtained from a truncated Taylor series expansion of the old flow about the old grid position $\underline{x}_0$. The subsequent analysis is carried out on the old grid, thus the indicators $\underline{x}_0$ are left out for brevity. ϕ refers to the old flow unless declared explicitly. The variational calculus according to Eqn. (15) is applied to the flow equations (10). As the RANS equations are satisfied for the old flow, the convective residual variations vanish identically and the variational RANS equations consist of local variations alone:

$$\delta R_i = 0 \qquad \text{and} \qquad \delta Q = 0 \qquad \text{in} \quad \Omega \tag{16}$$

Eqns. (16) govern the local flow variation corresponding to a particular shape perturbation. For incompressible flow the density shows no variation. A possible variation of the eddy-viscosity with respect to the shape is not taken into consideration, neither in terms of a convective nor a local variation. This frozen-turbulence assumption is common practice in industrial applications.[5,7]

As the shape variation originates from Γ_{dsg}, the boundary conditions on Γ_{dsg} are subject to both convective and local variations. The variational boundary condition is obtained by postulating that the original boundary condition also holds for the modified boundary. A

Dirichlet boundary condition postulated for the old flow $\phi^{(0)}$ on the old domain boundary $\underline{x}_0$ also needs to be satisfied by the new flow $\phi^{(1)}$ on the new position $\underline{x}_1$, viz.

$$\phi^{(0)}\big|_{\underline{x}_0} = \phi^{(1)}\big|_{\underline{x}_1} = \left[\phi^{(0)} + \delta\phi + \delta x_i \frac{\partial \phi^{(0)}}{\partial x_i}\right]_{\underline{x}_0} \quad \rightsquigarrow \quad \delta\phi = -\delta x_i \, \frac{\partial \phi^{(0)}}{\partial x_i} \quad \text{on} \quad \Gamma_{\text{dsg}} \,. \tag{17}$$

Variations of Neumann- and Robin-type boundary conditions can be derived accordingly.

4 ADJOINT RANS PROBLEM

The optimisation problem subject to the RANS equations can be turned into an unconstrained problem via the *Lagrangian calculus*. The objective functional is extended by the RANS constraints weighted by the Lagrange multipliers or adjoint variables $(\hat{U}_i,\, \hat{p})$

$$L = J + \int \mathrm{d}\Omega \left[\hat{U}_i \, R_i + \hat{p} \, Q\right] \,. \tag{18}$$

The adjoint variables are field variables, as their corresponding primal counterparts. Given that the RANS equations are satisfied for the reference case (design state investigated), this expression meets exactly the objective function value J. The gradient is obtained from the variation of the extended objective functional

$$\delta L = \delta J + \int_\Omega \mathrm{d}\Omega \left[\hat{U}_i \, \delta R_i + \hat{p} \, \delta Q\right] \,. \tag{19}$$

When the variational RANS constraints are satisfied, the variation of the Lagrangian matches the variation of the objective function. The strategy for the subsequent analysis is to chose the adjoint multipliers $(\hat{U}_i,\, \hat{p})$ such that any contribution to Eqn. (19) depending on local flow variations is eliminated. This particular choice $(\hat{U}_i,\, \hat{p})$ is found from the adjoint RANS equations, which are specific to the objective functional. After solving the adjoint problem for a certain objective function, the objective function derivatives are obtained by evaluating the remaining terms – for an arbitrary number of shape parameters

Integration by parts of Eqn. (19) yields the *adjoint field equations* and boundary conditions, which eliminate the local flow variations for arbitrary/admissible choices $(\delta U_i,\, \delta p)$. The adjoint field equations are

$$\begin{cases} -\rho \, U_j \dfrac{\partial \hat{U}_i}{\partial x_j} \;=\; \dfrac{\partial}{\partial x_j}\left(2\,\mu_{\text{eff}}\,\hat{S}_{ij} - \hat{p}\,\delta_{ij}\right) - \rho\,\hat{U}_j \dfrac{\partial U_j}{\partial x_i} - \dfrac{\partial j}{\partial U_i} & \text{in} \quad \Omega_{\text{obj}} \\ -\rho \, U_j \dfrac{\partial \hat{U}_i}{\partial x_j} \;=\; \dfrac{\partial}{\partial x_j}\left(2\,\mu_{\text{eff}}\,\hat{S}_{ij} - \hat{p}\,\delta_{ij}\right) - \rho\,\hat{U}_j \dfrac{\partial U_j}{\partial x_i} & \text{in} \quad \Omega \setminus \Omega_{\text{obj}} \end{cases} \tag{20}$$

and

$$\begin{cases} \dfrac{\partial \hat{U}_i}{\partial x_i} \;=\; \dfrac{\partial j}{\partial p} & \text{in} \quad \Omega_{\text{obj}} \\ \dfrac{\partial \hat{U}_i}{\partial x_i} \;=\; 0 & \text{in} \quad \Omega \setminus \Omega_{\text{obj}} \,, \end{cases} \tag{21}$$

with the variational objective function integrand

$$\delta j = \delta p \, \frac{\partial j}{\partial p} + \delta U_i \, \frac{\partial j}{\partial U_i} \, . \tag{22}$$

The corresponding adjoint boundary conditions are presented in Table 1.

Table 1: Summary of boundary conditions for the adjoint RANS equations.

boundary	$\hat{U}_t$	$\hat{U}_n$	$\hat{p}$
no-slip walls	$\hat{U}_t = 0$	$\hat{U}_n = 0$	$\hat{p}_{,n} = 0$
slip wall	$\hat{U}_{t,n} = 0$	$\hat{U}_n = 0$	$\hat{p}_{,n} = 0$
inflow	$\hat{U}_t = 0$	$\hat{U}_n = 0$	$\hat{p}_{,n} = 0$
pressure outflow	$\rho U_n \hat{U}_t + \mu_{\text{eff}} \hat{U}_{t,n} = 0$	$\hat{p} = \rho U_n \hat{U}_n + \mu_{\text{eff}} \hat{U}_{n,n}$	

For constant ship velocity U_S and frozen $\mathcal{D}_{II}$ the variation of the SVA criterion (7) with respect to the flow reads

$$\delta J_A = \int_{\Omega_{\text{obj}}} \mathrm{d}\Omega \, \frac{\partial j_A}{\partial U_i} \qquad \text{with} \qquad \frac{\partial j_A}{\partial U_i} = -\tilde{e}_i^a \, \frac{C_A}{2} \, \frac{U_a - \overline{U}_a(r)}{r} \, \sqrt{\frac{U_S \, \mathcal{D}_{II}(r)}{\left| U_a - \overline{U}_a(r) \right|^3}} \, . \tag{23}$$

For frozen $\overline{U}_a(r)$ the simplified formulation (9) immediately leads to

$$\delta J_B = \int_{\Omega_{\text{obj}}} \mathrm{d}\Omega \, \frac{\partial j_B}{\partial U_i} \qquad \text{with} \qquad \frac{\partial j_B}{\partial U_i} = -\tilde{e}_i^a \, C_B \, \frac{U_a - \overline{U}_a(r)}{r} \, . \tag{24}$$

Eqns. (23) and (24) can be considered as different weights applied to the deviation $[U_a - \overline{U}_a(r)]$.

Having eliminated the local flow variations by satisfying the adjoint RANS equations, the remaining terms of Eqn. (19) make the *adjoint sensitivity equation*. After some transformation the variation for boundary-normal shape perturbations, $\delta n = \delta \underline{x} \cdot \underline{n}$, becomes

$$\delta J = \int_{\Gamma_{\text{dsg}}} \mathrm{d}\Gamma \, [\mathcal{G} \, \delta n] \, , \tag{25}$$

with the gradient distribution

$$\mathcal{G} = \frac{1}{\mathrm{d}\Gamma} \frac{\delta J}{\delta n} = \frac{\delta J}{\delta V} = -\mu_{\text{eff}} \, \frac{\partial U_t}{\partial n} \, \frac{\partial \hat{U}_t}{\partial n} \, (\underline{t} \cdot \hat{\underline{t}}) \qquad \text{over} \quad \Gamma_{\text{dsg}} \, . \tag{26}$$

The in-plane boundary unit vectors for flow and adjoints are

$$t_i = n_j S_{ij} / \mathcal{S} \quad \text{and} \quad \hat{t}_i = n_j \hat{S}_{ij} / \hat{\mathcal{S}} \, , \quad \text{using} \quad \mathcal{S}^2 = 2 S_{ij} S_{ij} \quad \text{and} \quad \hat{\mathcal{S}}^2 = 2 \hat{S}_{ij} \hat{S}_{ij} \, .$$

The continuous gradient distribution, Eqn. (26), represents the sensitivity of the objective functional with respect to a volume change δV, positive [negative] for an increase in fluid [solid] volume.

5 PRIMAL AND ADJOINT RANS SOLVERS

The incompressible RANS equations are solved using a collocated cell-centred finite volume discretisation on fully unstructured grids with hanging grid nodes. The algorithm is parallelised based on the MPI protocol. Pressure-velocity coupling is enforced by the SIMPLE pressure correction scheme. The same approach is used for the adjoint code, i.e. Eqns. (20) and (21) are solved using an adapted SIMPLE scheme. The adjoint code is written closest possible to the primal RANS solver. Coding effort can significantly be reduced by reusing huge portions of the original solver (approx. 90 per cent in FreSCo$^+$). Consistency of both primal and adjoint discretisation (duality) minimises potential mismatches between the objective function values calculated by the primal solver and its variations obtained with the adjoint code. Due to the negative sign of the adjoint convection, the direction of the convective transport is opposite to the original PDE. Standard convection schemes, namely UDS-CDS blending, and TVD-based QUICK and LUDS formulations, have been adapted to the adjoint problem. The adjoint right-hand terms (20/21) depend on the definition of the objective function. Hence, the adjoint equations need to be solved once per objective function considered. The sensitivity equation (25) is evaluated after solving the adjoint equations in the adjoint post-processing. According to Eqn. (26), the shape sensitivities are obtained from a boundary formulation that does not require a mesh deformation. This is particularly important for unstructured-grid implementations.

The adjoint technique traces the sensitivity back from the objective volume(s) Ω_{obj} to the design surface(s) Γ_{dsg}. In other words, the information is backtracked from the receiver to the sender. This reverse or backwards strategy is reflected, for example, in the inverse convection direction of the adjoint equations.

6 TEST CASE

A simple submerged body is considered first in order to test the adjoint-based calculus. For symmetry reasons only one quarter is modelled. The geometry was created using the FRIENDSHIP FRAMEWORK. The case was set up at a length-based Reynolds number of $5 \cdot 10^5$ with prescribed velocities at the inlet. A wall boundary condition is applied on the hull using a logarithmic law of the wall. At the outlet we have used a pressure outflow condition at constant ambient pressure. The remaining boundaries are defined as symmetry planes. The computational domain extends two body lengths ahead, below and to the side. Three lengths are modelled in the wake direction. The grids of approx. 250 thousand cells were generated using the HEXPRESS mesh-generator. Several refinement boxes were defined together with a boundary layer mesh associated to the wetted hull surface. A snapshot of the surface grid over the aftship and the cells within the propeller disk is given in Fig. 1. The right-hand side term, $-\rho\hat{U}_j U_{j,i}$, appearing in the adjoint field Eqn. (20) was neglected for convergence reasons. We have chosen the SVA-criterion (7) to assess the design. The propeller disk radius is 10 per cent higher than the propeller radius and measures 10 per cent of the body length (without the shaft extension).

The sensitivity distribution over the hull was imposed on the original form with a step-width chosen intuitively. Fig. 2 contains the original hull form (black lines), the

recommendation according to the adjoint sensitivity analysis (green lines) and our modification guided by the sensitivities (red lines). Our deformation follows the general trends of the sensitivity derivatives. A re-evaluation of the modified geometry by the RANS solver yields $J_A = 0.809$ compared to the original value of $J_A = 0.778$. The wake distributions for 10 radii are provided in Fig. 3 – the original on the left, the modification on the right-hand side. The radial variation is reduced for the modified geometry, particularly on the outer radii. Due to the thickness of the propeller disk the results scatter over the ordinate. However, we believe that this will increase the robustness of the design.

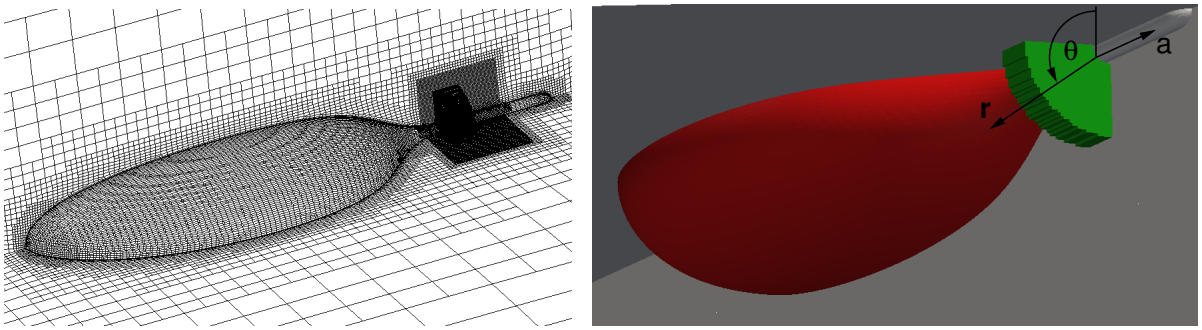

Figure 1: Left: Computational mesh used for the simple submerged body. In addition to the surface grid, the plot contains the volume cells in the propeller disk Ω_{obj}. Right: The design surface Γ_{dsg} is visualised in red, the propeller disk carrying the objective function volume Ω_{obj} in green.

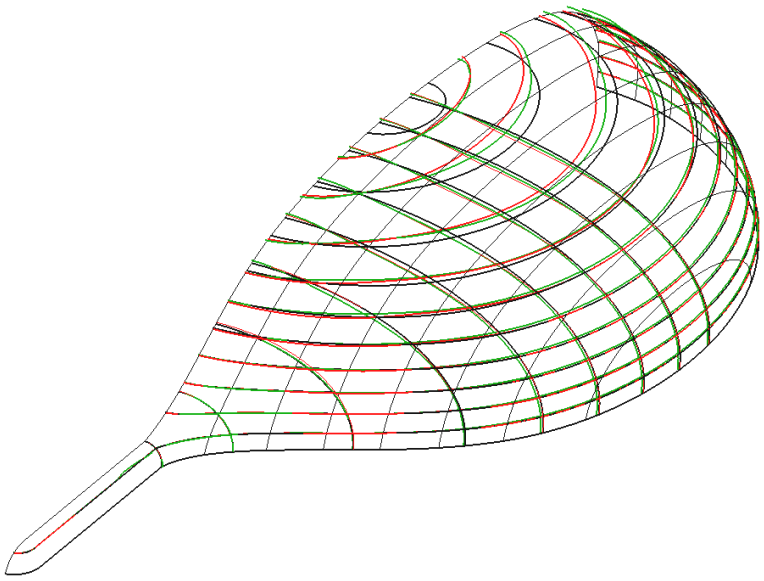

Figure 2: Original shape (black), sensitivity recommendation (green) and shape modifications (red). The applied shape modifications follow the main trends indicated by the shape sensitivities.

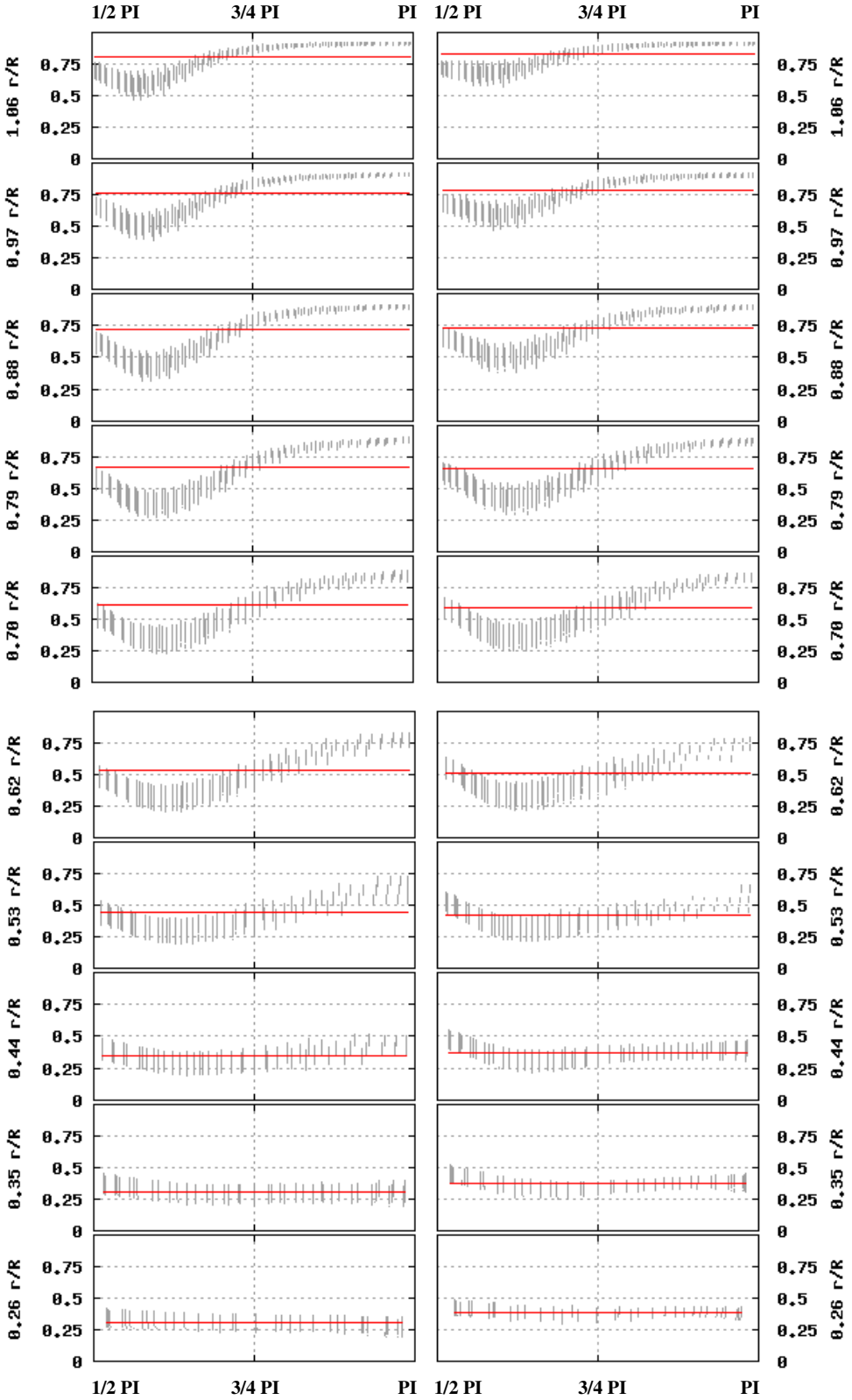

Figure 3: Circumferential distribution of the axial velocity U_a in the propeller disk for the submerged test body (original left, modification right). 10 radii have been chosen at different r/R_O positions. For symmetry reasons only a quarter is shown ranging from $\pi/2 < \theta < \pi$. The red line is the average value for the radius.

7 KRISO Container Ship (KCS)

The considered test case was conceived in 1997 at the Korea Research Institute for Ships and Ocean Engineering (KRISO). For a model-size container ship with a bulbous bow tank towing tests and self propulsion tests were carried out. It was chosen here as it is a widely-known well-studied test case. The KCS is characterised by a rather slender hull geometry. Compared to other ships it features a high wake quality and is considered a challenge for the optimisation study. The model's geometry is described in the IGES-format. Table 2 gives the main particulars of the testcase. The case was set up at model-scale at a

Table 2: Main particulars of the KCS Testcase

Speed [kn]	24.0
Length between perpendiculars LPP [m]	230.0
Length waterline WL [m]	232.5
Beam [m]	32.2
Draft [m]	10.8
Propeller diameter [m]	7.9
Block coefficient [-]	0.65050
Midship section coefficient [-]	0.98490
Propeller hub, long. location (x/LPP, aft of forward perp.) [m]	0.98250
Propeller hub, vert. location (-z/LPP, below waterline) [m]	0.02913

length-based Reynolds number of 10^7 with prescribed velocities at the inlet. A symmetry boundary condition is applied to bottom, top (still-watersurface), midship plane and the far side. At the outlet we have used a pressure outflow condition, where the pressure is set to ambient pressure. The computational domain extends one ship length ahead, below and to the side. Two ship lengths are modelled in the aft direction. The grids were generated using the HEXPRESS mesh-generator and have approx. 820 thousand cells. Several refinement boxes were defined together with a boundary layer mesh associated to the wetted hull surface. A snapshot of the surface grid over the aftship and the cells within the propeller disk is given in Fig. 4. The wall boundary layers are modelled via the logarithmic law of the wall. The wake objective function was evaluated in the propeller disk which measures 1.05 times the propeller diameter. The inner propeller disk diameter was set to 1.2 times the diameter of the shaft extension which is 1.48 m. The thickness of the propeller disk was 1 m.

According to Eqn. (20), the adjoint flow is driven by the so-called adjoint body-forces, $\partial j/\partial x_i$, acting inside the propeller disk volume Ω_{obj}. The corresponding adjoint velocity field inside the propeller disk is depicted in Fig. 5 together with the axial velocity of the flow. Areas of high deviation from the mean flow induce local adjoint velocities. The right-hand side term, $-\rho\hat{U}_j U_{j,i}$, appearing in the adjoint field Eqn. (20) was again neglected. It was found to cause convergence problems at $Re = 10^7$ particularly in combination with wall functions. The gradient distribution $\mathcal{G}$ is obtained over the complete hull surface

Γ_{dsg}. As shown in Fig. 6 the sensitivities have been imposed (red) on the original hull (black) using an arbitrary step-width. We followed the gradient direction in a manual re-design of the hull leading to considerable changes in the geometry. The modified hull was re-evaluated on the basis of a re-meshing strategy using the same control settings. The changes in the wake objective function ($J_A \approx 0.81$ for the reference case) were below 3 per mil. The sensitivities calculated for the modified geometry (see Fig. 7) are very close to the ones calculated for the initial design, indicating that a wider step-size could have been chosen. Usually the aftship design is subject to numerous constraints and fixed-points from engine installations and shafting etc. The degree of freedom is very limited so that we assume that the vessel is close to the local optimum feasible from a technical point of view.

8 CONCLUSIONS

The 3-D unstructured finite volume RANS solver FreSCo$^+$ has been extended by an adjoint solver in order to aid in the shape design of ship hulls. Wake objective functions used in practical hull design were introduced to the adjoint calculus and applied to both a simple immersed body and the KRISO container ship. The method yields considerable insight from the objective point of view, providing a continuous sensitivity distribution over the design surface.

A number of improvements will be required to prepare the adjoint technique for production use – among them:

- Provide the data interfaces to existing CAD/CAE frameworks.
- Extend the adjoint formulation to further cost functions.
- Optimise the adjoint solver (stability, numerical treatment of new terms).
- Improved turbulence treatment.

REFERENCES

[1] J. L. Lions, Optimal control of systems governed by partial differential equations, Springer-Verlag, New York (1971)

[2] O. Pironneau, On optimum design in fluid mechanics, *Journal of Fluid mechanics*, **64** (1974)

[3] A. Jameson, Optimum Aerodynamic Design Using CFD and Control Theory, AIAA-1995-1729-807, 12th AIAA Computational Fluid Dynamics Conference (1995)

[4] H. Söding, Hull Shape Design for Reduced Resistance, *Ship Research Technology*, **48**, 135–144 (2001)

[5] O. Soto and R. Löhner, On the Computation of Flow Sensitivities From Boundary Integrals, AIAA-2004-0112, 42th AIAA Aerospace Sciences Meeting and Exhibit, Reno, Nevada (2004)

[6] O. Soto, R. Löhner and C. Yang, An adjoint-based design methodology for CFD problems, *International Journal of Numerical Methods for Heat & Fluid Flow*, **14**, 734–759 (2004)

[7] C. Othmer, A continuous adjoint formulation for the computation of topological and surface sensitivities of ducted flows, *International Journal for Numerical Methods in Fluids*, **58**, 861–877 (2008)

[8] A. Stück and T. Rung, Adjoint RANS for Hull-Form Optimisation, *12th Numerical Towing Tank Symposium*, NuTTS 2009, Cortona, Italy (2009)

[9] Schiffbau-Versuchsanstalt Potsdam GmBH, *Bericht Nr. 1714* (in german)

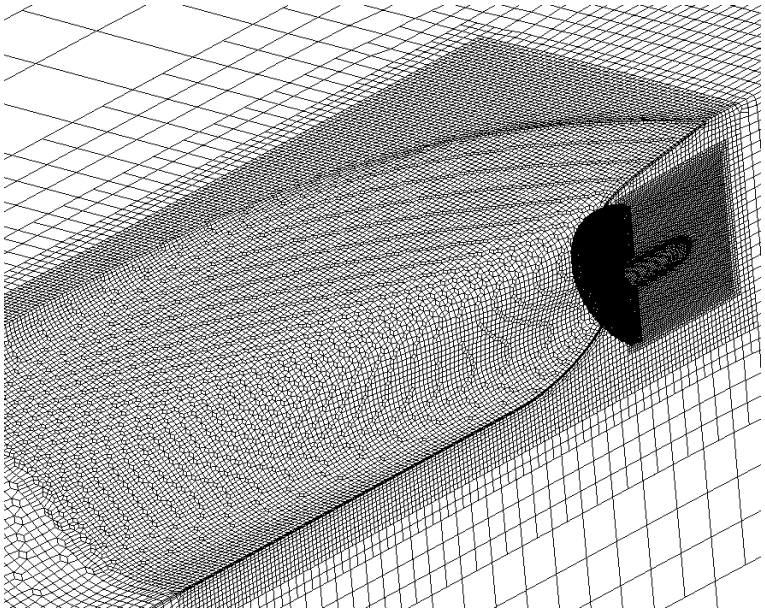

Figure 4: Computational grid used for the KCS, $Re = 10^7$. Besides the surface grid, the volume cells in the propeller disk Ω_{obj} are presented.

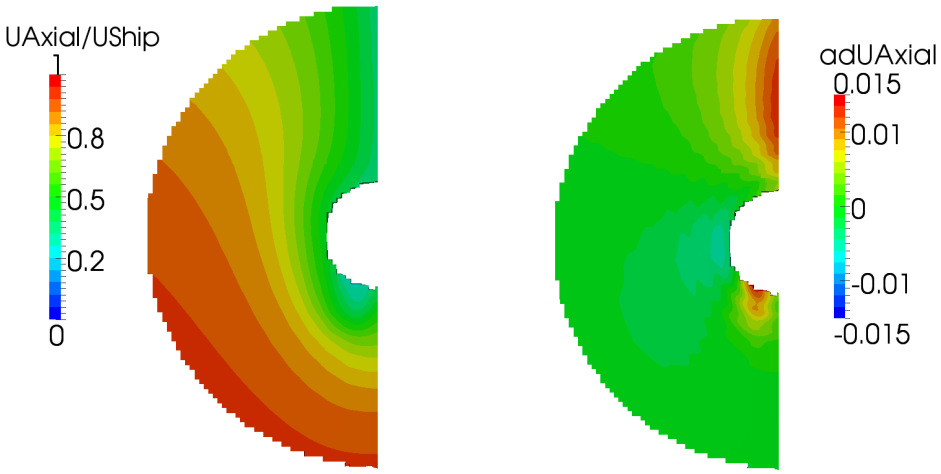

Figure 5: Normalised axial velocity distribution in the propeller disk for the KCS (left). Corresponding adjoint velocity field (right).

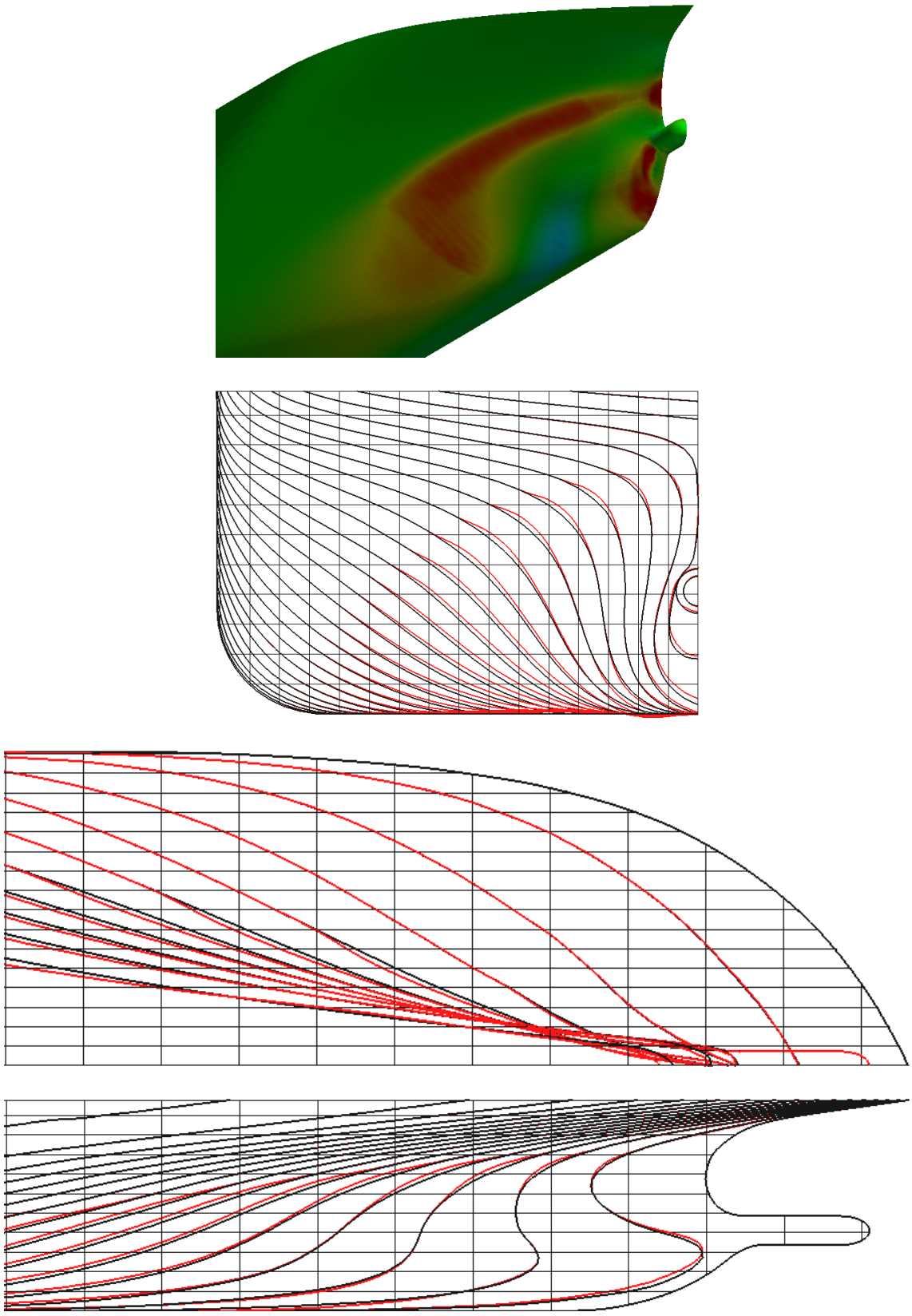

Figure 6: Reference configuration. On top: Sensitivity derivatives (red=inwards, blue=outwards). The sensitivity derivatives were imposed (red) to the original KCS geometry (black) using an arbitrary step-width. Frames, waterlines and buttock-lines (top-down).

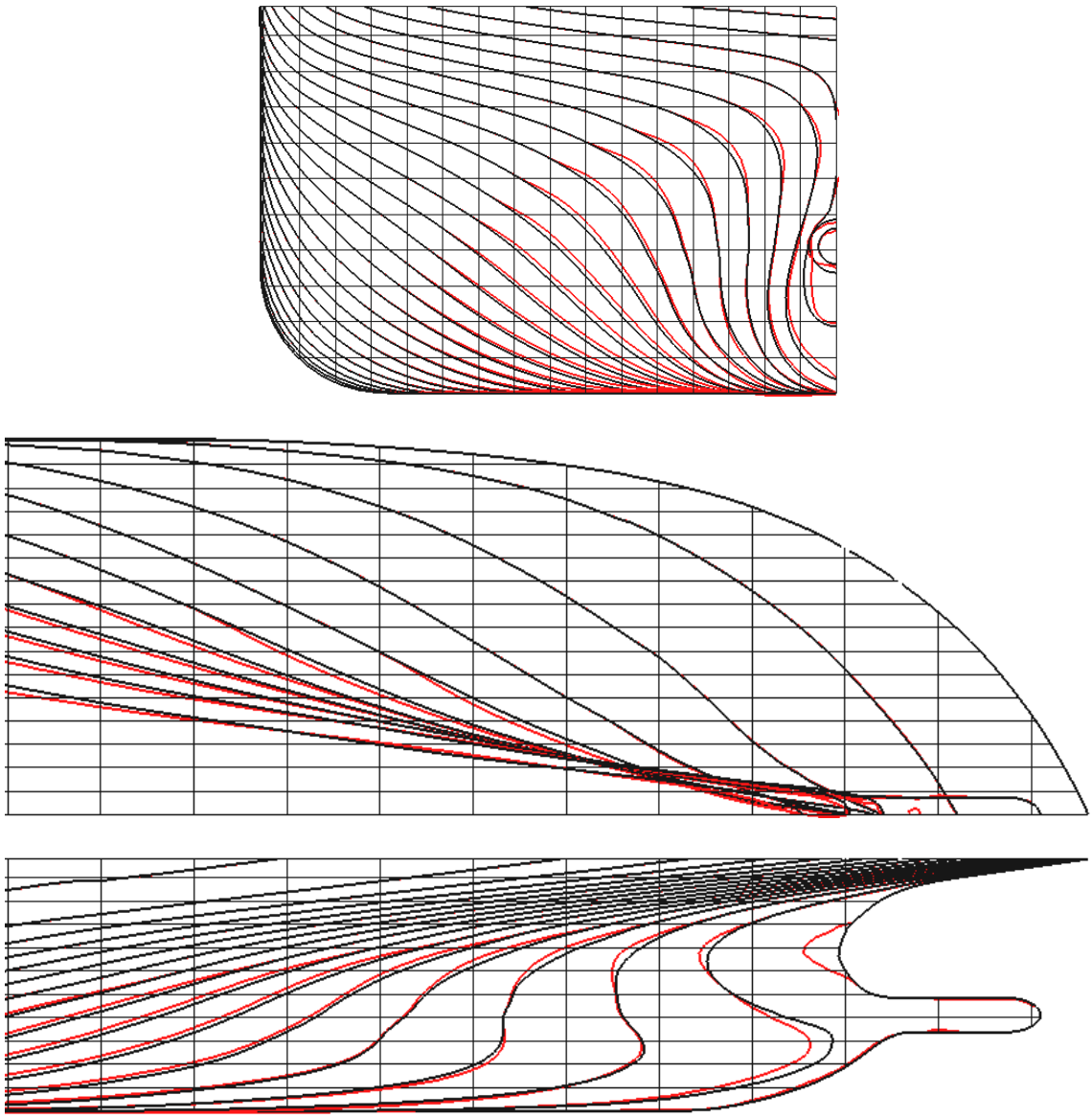

Figure 7: First design cycle: Sensitivity derivatives imposed (red) to the modified KCS geometry (black) using an arbitrary step-width. Frames, waterlines and buttock-lines (top-down).